REPORT DOCUMENTATION PAGE

Public reporting burden for this collection of information is estimated to average 1 hour per response, including the time for reviewing instructions, searching existing data sources, gathering and maintaining the data needed, and completing and reviewing this collection of information. Send comments regarding this burden estimate or any other aspect of this collection of information, including suggestions for reducing this burden to Department of Defense, Washington Headquarters Services, Directorate for Information Operations and Reports (0704-0188), 1215 Jefferson Davis Highway, Suite 1204, Arlington, VA 22202-4302. Respondents should be aware that notwithstanding any other provision of law, no person shall be subject to any penalty for failing to comply with a collection of information if it does not display a currently valid OMB control number. **PLEASE DO NOT RETURN YOUR FORM TO THE ABOVE ADDRESS.**

1. REPORT DATE *(DD-MM-YYYY)* 30-01-2012	2. REPORT TYPE Final	3. DATES COVERED *(From - To)* April 2009 - January 2012

4. TITLE AND SUBTITLE

Numerical simulation and forecast of equatorial spread F under realistic postsunset conditions

5a. CONTRACT NUMBER

5b. GRANT NUMBER
FA9550-09-1-0337

5c. PROGRAM ELEMENT NUMBER

6. AUTHOR(S)

D. L. Hysell and H. A. Aveiro

5d. PROJECT NUMBER

5e. TASK NUMBER

5f. WORK UNIT NUMBER

7. PERFORMING ORGANIZATION NAME(S) AND ADDRESS(ES)

Cornell University
Earth and Atmospheric Sciences
3114 Snee Hall
Ithaca, NY 14853

8. PERFORMING ORGANIZATION REPORT NUMBER

9. SPONSORING / MONITORING AGENCY NAME(S) AND ADDRESS(ES)

Air Force Office of Scientific Research
Physics and Electronics (NE)
DCT, Space Situational Awareness
875 N. Randolph St.
Arlington, VA 22203

10. SPONSOR/MONITOR'S ACRONYM(S)

AFOSR

11. SPONSOR/MONITOR'S REPORT NUMBER(S)
AFRL-OSR-VA-TR-2012-0539

12. DISTRIBUTION / AVAILABILITY STATEMENT

A

13. SUPPLEMENTARY NOTES

See attached PDF for detail.

14. ABSTRACT

A fully three-dimensional numerical simulation of plasma density irregularities in the postsunset equatorial F region ionosphere leading to equatorial spread F (ESF) has been developed. The simulation evolves under realistic background conditions including bottomside plasma shear flow and vertical current. It has been initialized and driven in accordance with background measurements obtained from the Air Force C/NOFS satellite, the Jicamarca Radio Observatory, the Altair radar on Kwajalein, and other instruments. Simulations are seeded with white noise alone and are, in that sense, agnostic with respect to the required, underlying seed mechanism. A combination of generalized Rayleigh Taylor (gRT) and collisional shear instability (CSI) has been found to produce growing waveforms with key features that agree with satellite and ground-based radar observations in several important respects, including their gross morphology, development rates, and magnetic signatures. The transient response of CSI is consistent with the observation of bottomside waves with wavelengths close to 30 km, whereas the steady-state behavior of the combined instability can account for the 100+ km wavelength waves that predominate in the F region.

15. SUBJECT TERMS

16. SECURITY CLASSIFICATION OF:			17. LIMITATION OF ABSTRACT	18. NUMBER OF PAGES	19a. NAME OF RESPONSIBLE PERSON
a. REPORT	b. ABSTRACT	c. THIS PAGE		16	19b. TELEPHONE NUMBER *(include area code)*

Final Report: Numerical Simulation and Forecast of Equatorial Spread F under Realistic Postsunset Conditions
Grant/Contract Number: FA9550-09-1-0337

D. L. Hysell and H. C. Aveiro
Earth and Atmospheric Sciences
Cornell University

January 30, 2012

Abstract

A fully three-dimensional numerical simulation of plasma density irregularities in the postsunset equatorial F region ionosphere leading to equatorial spread F (ESF) has been developed. The simulation evolves under realistic background conditions including bottomside plasma shear flow and vertical current. It has been initialized and driven in accordance with background measurements obtained from the Air Force C/NOFS satellite, the Jicamarca Radio Observatory, the Altair radar on Kwajalein, and other instruments. Simulations are seeded with white noise alone and are, in that sense, agnostic with respect to the required, underlying seed mechanism. A combination of generalized Rayleigh Taylor (gRT) and collisional shear instability (CSI) has been found to produce growing waveforms with key features that agree with satellite and ground-based radar observations in several important respects, including their gross morphology, development rates, and magnetic signatures. The transient response of CSI is consistent with the observation of bottomside waves with wavelengths close to 30 km, whereas the steady-state behavior of the combined instability can account for the 100+ km wavelength waves that predominate in the F region.

Introduction

The goal of the Air Force C/NOFS satellite mission is to forecast radio propagation disruptions caused by plasma irregularities formed during equatorial spread F conditions. The AFRL methodology involves using data from the C/NOFS satellite and elsewhere to initialize large-scale simulations of the background equatorial ionosphere, let them evolve in time, and estimate the likelihood of instability by evaluating estimators of the linear growth rate of the generalized Rayleigh Taylor (GRT) instability. When and where elevated growth rates are detected, intermediate-scale simulations are run to predict irregularity development, extent, and morphology and to predict radio scintillation levels. Readers may consult *Retterer* [2005]; *Retterer et al.* [2005] for details.

However, sounding rocket experiments on Kwajalein, radar measurements from Altair and Jicamarca, and numerical simulations from the Cornell group argue that an important intermediate process is involved in initiating ESF. At issue are plasma instabilities that grow in the bottomside F and valley regions, at the base of a stratum of strong plasma shear where plasma and neutral drifts are antiparallel (retrograde). The growth rate of these "collisional shear" instabilities (CSI) is predicted to be several times faster than GRT, and the preferred scale sizes of the waveforms it produces match those of the large-scale waves observed at the onset of ESF. Understanding and modeling these instabilities would appear to be a crucial step in forecasting spread F.

Under AFOSR support, we developed a simulation code that includes both CSI and GRT instability. Together, these processes exhibit rapid growth and other emergent behavior (characteristics exhibited by neither one acting alone) [*Aveiro and Hysell*, 2010]. ESF depletions generated by the simulation under realistic background driving conditions were morphologically similar to typical Jicamarca observations. Simulations driven by C/NOFS-supplied electric fields produced ESF plumes that matched, quantitatively and qualitatively, radar observations from Altair [*Aveiro et al.*, 2011].

Below, we review representative C/NOFS and Altair radar observations of ESF irregularities and show how the salient features of the observations have been recovered by our numerical simulations of the phenomena. The simulation results are sufficiently similar to the observations to inspire considerable confidence regarding their predictive capability.

Representative Radar Observations

The ARPA Long-Range Tracking and Instrumentation Radar (ALTAIR) is a VHF/UHF radar located at Kwajalein Atoll (8.8°N, 167.5°E) [*Tsunoda et al.*, 1979]. Figure 1 displays ALTAIR UHF (422 MHz) data for the night of April 29, 2009. ALTAIR observations made perpendicular to the geomagnetic field at F region heights represent a combination of coherent and incoherent scatter, whereas off-perpendicular scans reflect only incoherent scatter.

The top panel of Figure 1 shows ALTAIR scans made pointing perpendicular to the geomagnetic field around 09:45 UT (LT $\approx$ UT+11 hr in the radar longitudinal sector). By this time, irregularities had formed at the base of the F region as bottom-type layers. These were patchy and spaced by about 35 km. They are common precursors of fully-developed ESF, whereas bottom-type layers tend to be more continuous (beam-filling) or absent on nights when topside ESF does not develop [*Hysell et al.*, 2004].

ALTAIR scans made pointing off-perpendicular to the geomagnetic field at 10:30 UT and 11:26 UT are shown in the middle and bottom panels of Figure 1, respectively. By about 10:30 UT, the irregularities were still confined to the base of the F region, but the predominant horizontal scale had increased to 100-200 km. Between about 10:30 and 11:26 UT, the bottomside depletions underwent strong vertical development. Depleted channels penetrated to the topside while retaining their 100-200 km horizontal spacing. The depletions had characteristic tilts and showed evidence of bifurcation and secondary instabilities. Wedges of enhanced plasma also appeared to be driven downward in between ascending depletions.
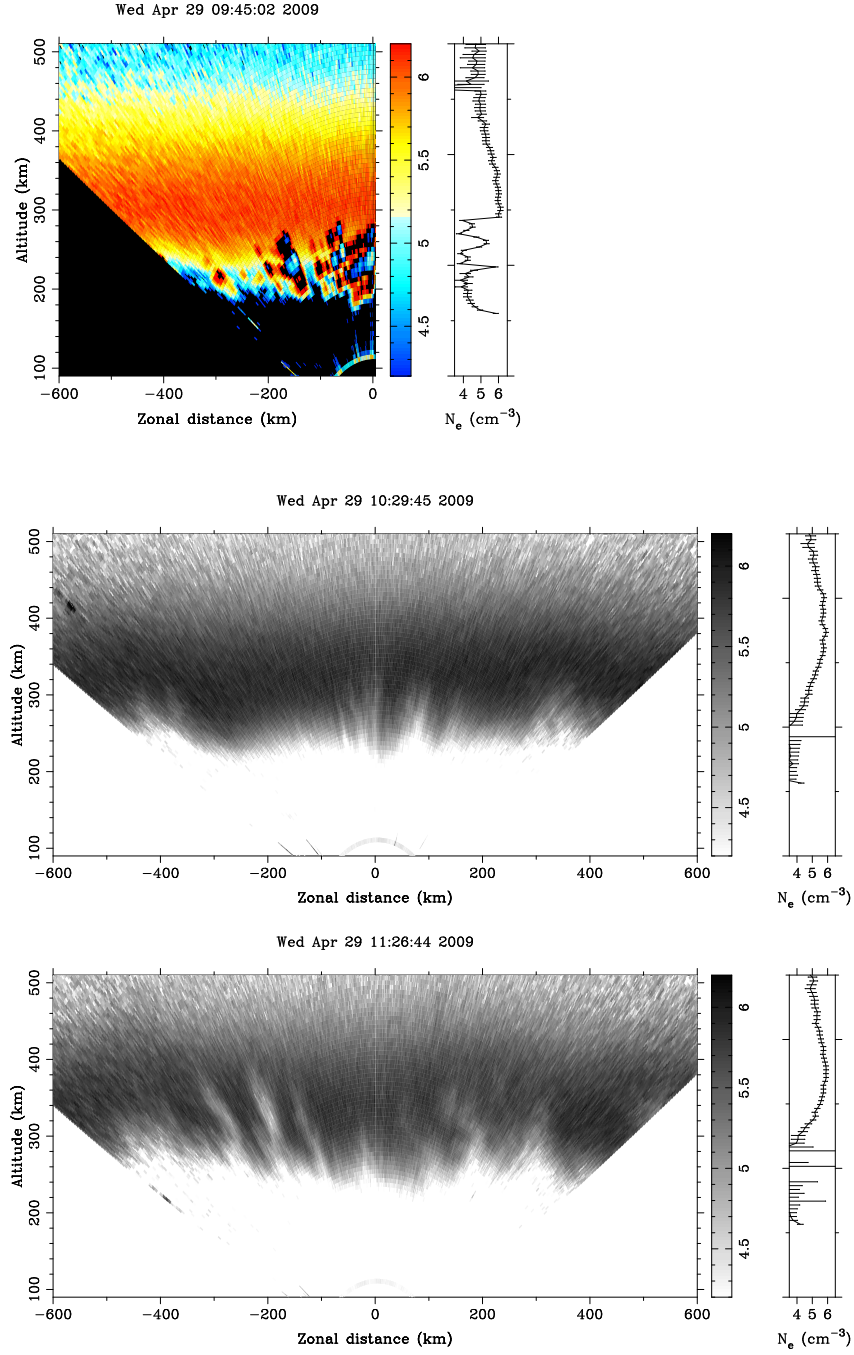
Figure 1: ALTAIR radar scans for April 29, 2009, showing backscatter power, range corrected and scaled to electron density on a logarithmic scale: (top) perpendicular scan at 09:45 UT, off-perpendicular scans at (middle) 10:30 UT and (bottom) 11:26 UT. The rightmost panels depict vertical electron density profiles. Note that LT ≈ UT + 11 hr.

Representative Satellite Observations

To drive simulations of the April 29, 2009 ESF event, *in situ* electric field measurements from the Ion Velocity Meter (IVM) and Vector Electric Field Instrument (VEFI) on board the Communications/Navigation Outage Forecasting System (C/NOFS) satellite were used. IVM is comprised of an ion drift meter and an ion-retarding potential analyzer that together provide measurements of the ion drift vector, the ion temperature, and the major ion composition. The VEFI instrument consists of an electric field meter, a fluxgate magnetometer, an optical lightning detector, and a fixed-bias Langmuir probe. Among its products are measurements of DC, quasi-DC, and AC electric fields.

Figure 2 shows the zonal electric field (based on IVM ion drift and VEFI magnetometer measurements) and (IVM) ion density measurements with the respective orbital information tabulated below (geographic and magnetic coordinates, altitude, and universal and solar local times). The results correspond to C/NOFS passes during the post-sunset period on April 29, 2009, centered at the Kwajalein longitudinal sector. For comparison, satellite passes at (top panels) $\sim$ 09:03 UT, (middle panels) $\sim$ 10:47 UT and (bottom panels) $\sim$ 12:31 UT are shown.

During the first C/NOFS pass at about 09:03 UT, the zonal electric field was essentially zero, and no density or electric field perturbations were detected in the altitude range between 495-520 km. By the time of the next pass at about 10:47 UT, the zonal electric field had increased to 0.5-0.75 mV/m, and small electric field irregularities were emerging between 435-450 km altitude. That the background plasma density increased as the satellite altitude decreased suggests that it was flying in the topside, which is consistent with the evidence of Figure 1.

By the time the satellite passed through the Kwajalein sector again at about 12:30 UT, the electric field irregularities had become large (up to about 4 mV/m). Modest plasma density irregularities were also present at altitudes near 400 km. In view of Figure 1, however, the satellite most likely flew just above the most intense plasma density irregularities.

Numerical Model and Simulations

Here, we describe our numerical scheme for the simulation of the plasma density irregularities in the equatorial spread F event. The 3-D simulation updates the plasma density and electrostatic potential in time assuming quasineutrality and momentum balance. Inertia is neglected in the present incarnation. The characteristics of the neutral atmosphere are imported from empirical models. The background electric field is specified and controls the forcing. Simulations are performed with realistic background conditions including bottomside plasma shear flow and the attendant vertical current.

Rather than assuming equipotential magnetic field lines, the simulation solves the potential equation in three dimensions, allowing us to keep track of the distribution of parallel currents forced by the dynamos and of their closure. This also accommodates the possible effects of drift waves and related instabilities that may play secondary roles in ESF [*Huba and Ossakow*, 1979], [*LaBelle et al.*, 1986], [*Hysell et al.*, 2002]. For instance, the full 3-D treatment of warm plasma shows that perturbations on the surface of ionospheric plasma clouds propagate and twist into a barber pole configuration [*Drake and Huba*, 1987], [*Drake et al.*, 1988], [*Zalesak et al.*, 1990]. As a consequence, the phase of the corrugations varies strongly along $\mathbf{B}$, the plasma cloud loses its flute-like characteristic (i.e., $\mathbf{k} \cdot \mathbf{B} \neq 0$), and the resulting finite $k_{\parallel}$ has a dissipative influence on the instability. We do not know the extent to which similar phenomenon might affect the ESF development, but a study is underway. Finally, it is worth mentioning that magnetic field lines cease to be equipotentials near the bottom of the E region, decoupling the plasma and decreasing the conductive loading on the dynamo, which may influence the overall circulation.
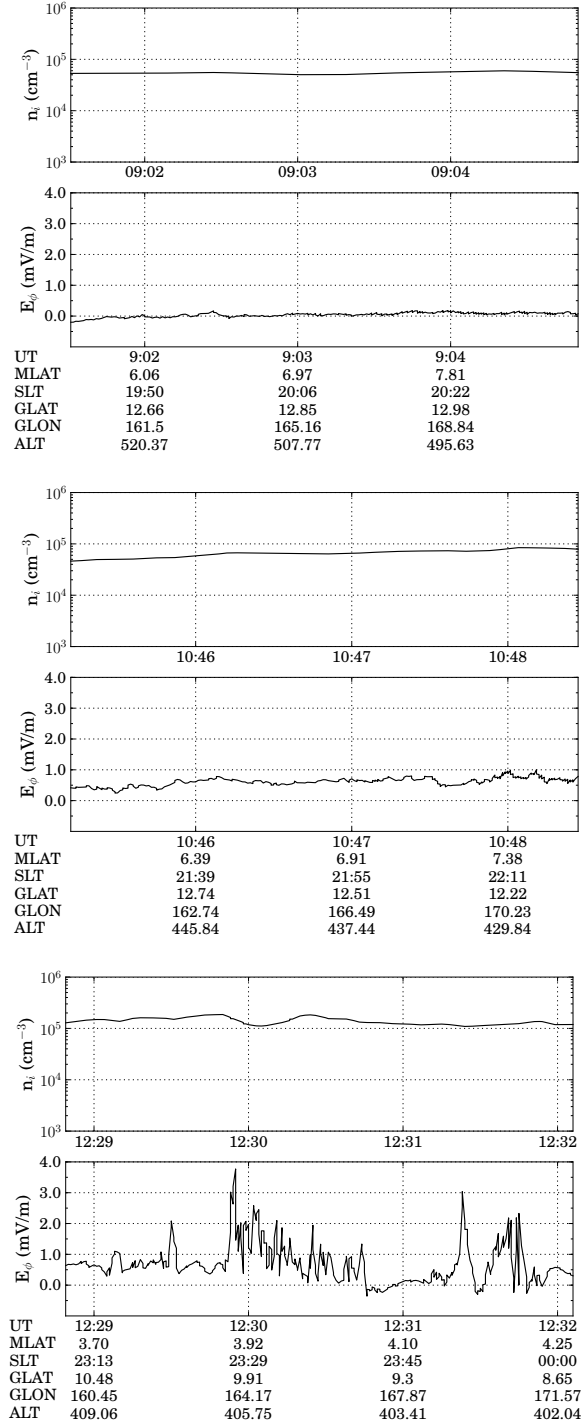
Figure 2: Ion density (cm^{-3}) and zonal electric field (mV/m) at three different passes through the Kwajalein sector: (top panel) $\sim$ 0903 UT, (middle panel) $\sim$ 1047 UT, and (bottom panel) $\sim$ 1230 UT. The tabulated entries are universal time (UT), magnetic latitude (MLAT), solar local time (SLT), geographic latitude (GLAT), longitude (GLON), and altitude (ALT) in km.

Conservation Laws

Neglecting stress, heat flow, and inertia, the fluid continuity equation and momentum equations for electrons and ions are given as:

$$\frac{\partial n_\alpha}{\partial t} + \nabla \cdot (n_\alpha \mathbf{v}_\alpha) = P_\alpha - L_\alpha, \tag{1}$$

$$\begin{aligned}
0 = \quad & - \quad \nabla p_\alpha + n_\alpha q_\alpha (\mathbf{E} + \mathbf{v}_\alpha \times \mathbf{B}) \\
& + \quad m_\alpha n_\alpha [\mathbf{g} - \nu_{\alpha n}(\mathbf{v}_\alpha - \mathbf{U}) - \sum_\beta^{\alpha \neq \beta} \nu_{\alpha\beta}(\mathbf{v}_\alpha - \mathbf{v}_\beta)],
\end{aligned} \tag{2}$$

where $p_\alpha = n_\alpha k_B T_\alpha$ is the pressure. The variables n_α, q_α, m_α, T_α, P_α, L_α, and $\mathbf{v}_\alpha$ are number density, electric charge, mass, temperature, production and loss rates, and velocity of the species α, respectively. The loss term includes charge exchange and dissociative recombination for a given species. Nighttime photoionization is neglected, but production due to charge exchange is considered. Here, β represents the other ionized bodies that exchange momentum or energy with α. The terms $\nu_{\alpha\beta}$ and $\nu_{\alpha n}$ are the collision frequencies with charged particles and neutrals, respectively. The terms $\mathbf{E}$, $\mathbf{B}$, $\mathbf{U}$, $\mathbf{g}$, and k_B represent the electric field, magnetic field, neutral wind, gravity, and the Boltzmann constant, respectively. Equation 1 is not in conservation form, since it includes chemical processes. However, it can be converted to conservative form through variable transformation. Two simplifications are applied to Equation 1 and Equation 2: (a) the neglect of diagmagnetic drifts ($\nabla n_\alpha \times \mathbf{B}$), since their associated flux divergence is very small when compared to the other terms, and (b) Coulomb collisions (the last term in the RHS of Equation 2) are treated implicitly and only included in the parallel direction.

Numerical Scheme

The simulation algorithm performs two computations. First, the self-consistent electric field is found using a 3-D potential solver based on quasineutrality, which can be expressed as

$$\nabla \cdot \left[\hat{\Sigma} \cdot \nabla \Phi \right] = \nabla \cdot \left[\hat{\Sigma} \cdot (\mathbf{E}_o + \mathbf{U} \times \mathbf{B}) + \hat{D} \cdot \nabla n + \hat{\Xi} \cdot \mathbf{g} \right] \tag{3}$$

where $\mathbf{E}_o$ is the background electric field, $\hat{\Sigma}$ is the conductivity tensor, $\hat{D}$ includes the diffusivity tensor, $\hat{\Xi} \cdot \mathbf{g}$ is gravity-driven current density, and Φ is the electrostatic potential that must arise to preserve a solenoidal current density. Explicit definitions of the tensors are given in *Shume et al.* [2005]. Note that the resulting electric field is the combination of the background and electrostatic fields (i.e., $\mathbf{E} = \mathbf{E}_o - \nabla \Phi$). Equation 3 involves a partial differential equation for the potential in three dimensions. It is solved using the BiConjugate Gradient Stabilized (BiCGStab) method (e.g. *van der Vorst* [1992]) using the algorithms described by *Saad* [1990].

Second, we solve a discretized version of Equation 1 for each ion species using a monotone upwind scheme for conservation laws (MUSCL) (a pedagogical review can be found in *Trac and Pen* [2003]) directly applicable to the ion continuity problem (once the recombination term has been absorbed into a redefinition of n_α so that Equation 1 becomes a conservation equation, as necessary). The characteristic of the neutral atmosphere (densities, temperature, and wind velocity) are updated in time on the basis of inputs from climatological models. The background electric field is specified and partly controls the forcing. The ion composition includes O^+, NO^+, and O_2^+. The model was constructed using tilted magnetic dipole coordinates (p, q, ϕ), where the tilt is matched to the magnetic declination in the longitude of interest. In our terminology, p represents the McIlwain parameter (L), q is the magnetic co-latitude, and ϕ is longitude (see e.g., *Hysell et al.* [2004]).

Empirical Model Drivers

To initialize the model runs, we derive plasma number densities from the Parametrized Ionospheric Model (PIM), a parametrization of the output of several regional theoretical model outputs generated for different climatological conditions and tuned somewhat to agree with data from Jicamarca and elsewhere [*Daniell et al.*, 1995]. PIM reproduces electron density profiles from Kwajalein and Jicamarca fairly closely if scaled slightly to account for day-to-day variability [*Aveiro and Hysell*, 2010]. The background number density profiles used for initial conditions are intended to reproduce measurements from ALTAIR, including the F region peak height and peak density, the bottomside density scale height, and the density in the valley region.

Plasma mobilities are calculated using neutral composition and temperature estimates from the Mass Spectrometer and Incoherent Scatter (NRL-MSISE00) model [*Picone et al.*, 2002] and ionospheric composition estimates from the International Reference Ionosphere (IRI-2007) model [*Bilitza and Reinisch*, 2008]. We take the ionosphere and neutral atmosphere to be in thermodynamic equilibrium after sunset ($T_n = T_e = T_i$). Expressions for the ion-neutral and electron-neutral collision frequencies used to compute conductivities can be taken from *Richmond* [1972]. Expressions for the Pedersen, Hall, and direct mobilities and diffusivities themselves are found in *Kelley* [2009], for example.

For our runs, the zonal neutral winds are obtained from the Horizontal Wind Model (HWM-07) [*Drob*, 2008]. As with PIM, these may be tuned slightly to account for day-to-day variability. The model is sensitive to the wind speeds throughout the thermosphere, since the growth rate of the collisional shear instability depends on the counter streaming flow of the neutrals and plasma. Meridional and vertical winds were neglected in the simulations presented here.

Simulation Initialization

Our simulation was cast on a rectangular grid $139{\times}133{\times}189$ points wide in (p, q, ϕ) space constructed using a tilted magnetic dipole coordinate system. A cut through the equatorial plane spans altitudes between 90–510 km and longitudes between $\pm\ 6°$. The flux tubes covered by the parallel coordinate all reach to the lower E region. The runs shown in this section are centered on the dip equator near Kwajalein (5.5° N latitude, 166.5° E longitude, 7.4° declination) with background conditions modeled for April 29, 2009. To seed the simulation run, we added independent Gaussian white noise to the initial number density with a 20% relative amplitude. The local time dependence of the background zonal electric field (E_ϕ) was estimated using measurements from IVM and VEFI on board the C/NOFS satellite. E_ϕ was taken to be constant in the F region but its amplitude is reduced below the valley to avoid the growth of electrojet gradient-drift instabilities. Based on those measurements E_ϕ was modeled as 0 mV/m before 21:00 LT, and 0.75 mV/m after 22:00 LT with a gradual transition using a hyperbolic tangent function in between. For example, E_ϕ=34 μV/m on the western boundary and 0.75 mV/m on the eastern boundary of the simulation by 10:40 UT, since those locations represent 21:22 LT and 22:10 LT, respectively.

Simulation Results

The initial conditions of our simulation at $t_\circ$=9:30 UT ($\approx$20:30 LT for the Kwajalein sector) are shown in Figure 3. The top panel shows the background plasma density. The initial conditions are consistent with ALTAIR radar observations for April 29, 2009, at that time. The middle panel of Figure 3 shows the perpendicular current density with the magnitude and direction indicated by the color disc in the lower panel. There are two major components to the current density that are combined in this depiction. First, a zonally eastward current driven by gravity exists throughout the region, showing a maximum at the F peak near 330 km altitude. In addition, a zonally eastward F region wind drives a vertical upward current in the region above about 200 km. The empirically modeled wind is almost constant with altitude, and thus the vertical current scales like the background ion density, showing a peak near 330 km and a strong vertical

gradient in the bottomside between 280 km and 240 km altitude. Below 150 km, the current is influenced by both the local zonal winds and the enhancement of the zonal current in the electrojet.

The divergence in the vertical current density is supported by a vertical electric field shown to the right of the middle panel. Above the bottomside, the field is directed downward, consistent with an eastward $\mathbf{E} \times \mathbf{B}$ drift in the same direction as the dynamo wind. Across the bottomside, the vertical electric field changes direction, producing a sheared zonal $\mathbf{E} \times \mathbf{B}$ drift, which provides free energy for the CSI below the shear node due to the differential velocity between plasma and neutrals.

The bottom panel of Figure 3 shows equatorward currents in both hemispheres on field lines that thread the bottomside in the altitude range from 250 km to 280 km. These currents feed the upward current driven by the F region zonal wind seen in the middle panel. Above the bottomside, the meridional current is distributed across all the field lines and is poleward in both hemispheres, serving to close the current loop driven by the F region dynamo.

Figure 4 shows the results for times matching, roughly, the three ALTAIR scans and C/NOFS passes. Note that the vertical axes indicate the apex altitude, i.e., the altitude mapped to the magnetic equator. For example, the magnetic field line that crosses over Kwajalein at 380 km altitude maps to 400 km altitude at the magnetic equator.

The top panel of Figure 4 depicts the evolution of ionospheric irregularities in the absence of a background electric field due entirely to the collisional shear instability. The spatial scales of the irregularities forming at the base of the bottomside range between 30–50 km. These irregularities cannot undergo vertical development and remain confined to altitudes where the plasma flow is retrograde.

By the time of the second panel in Figure 4, the transient phase of the CSI was ending, and the asymptotic phase was underway. The 30–50 km waves at the base of the bottomside had coalesced into large-scale waves with scale sizes between 100-200 km. Under the action of an increasing background zonal electric field, the bottomside irregularities begin to exhibit vertical development, more so on the eastern side of the simulation volume, which had experienced an eastward background electric field for more time.

In the final panel of the simulation, under the influence of a significant background electric field, the irregularities penetrate to the topside where gravity-driven currents can contribute further to growth. Some of the original intermediate scale structure from the first panel in the simulation survive, contributing to the overall fine structure. Bifurcation is evident, as well as secondary instabilities growing mainly on the westward walls of the primaries. Some descending, wedge-shaped plasma enhancements accompany the ascending depletions. The characteristic westward tilt of the irregularities is associated with the combination of vertical and zonal current and the combined CSI and gRT instabilities. As the simulation was initialized with white noise, and as gRT is a universal instability (nearly scale-size independent), the scale sizes of the irregularities evident here are a consequence of CSI.

Had a satellite passed through the simulated ionosphere at 379 km altitude over the Kwajalein sector ($\sim$400 km apex altitude) at about 11:13 UT, the electron density and electric field perturbations would have appeared as shown in Figure 5. Plasma depletions are present preferentially in the eastern half of the simulation grid. The western walls of the irregularities have steeper density gradients than the eastern walls. Perturbations in the zonal electric fields of the order 3-5 mV/m are present, collocated with large and small plasma depletions alike. Since the pass is a few kilometers above the top of most of the plasma depletions, relative perturbations in the density are small in all but one case, but the fringing fields penetrate to higher altitudes and are detectable in all cases.

Overall Findings

In simulation, the combination of CSI and gRT produced growing waveforms with characteristics that matched the observations made by ALTAIR radar. The dominant plasma irregularities with (initially) decakilometric-scale took approximately 100min to evolve from the bottomside up to the F peak. By the time they reached the F peak, they had coalesced into waveforms with 100 km+ scale sizes. This behavior
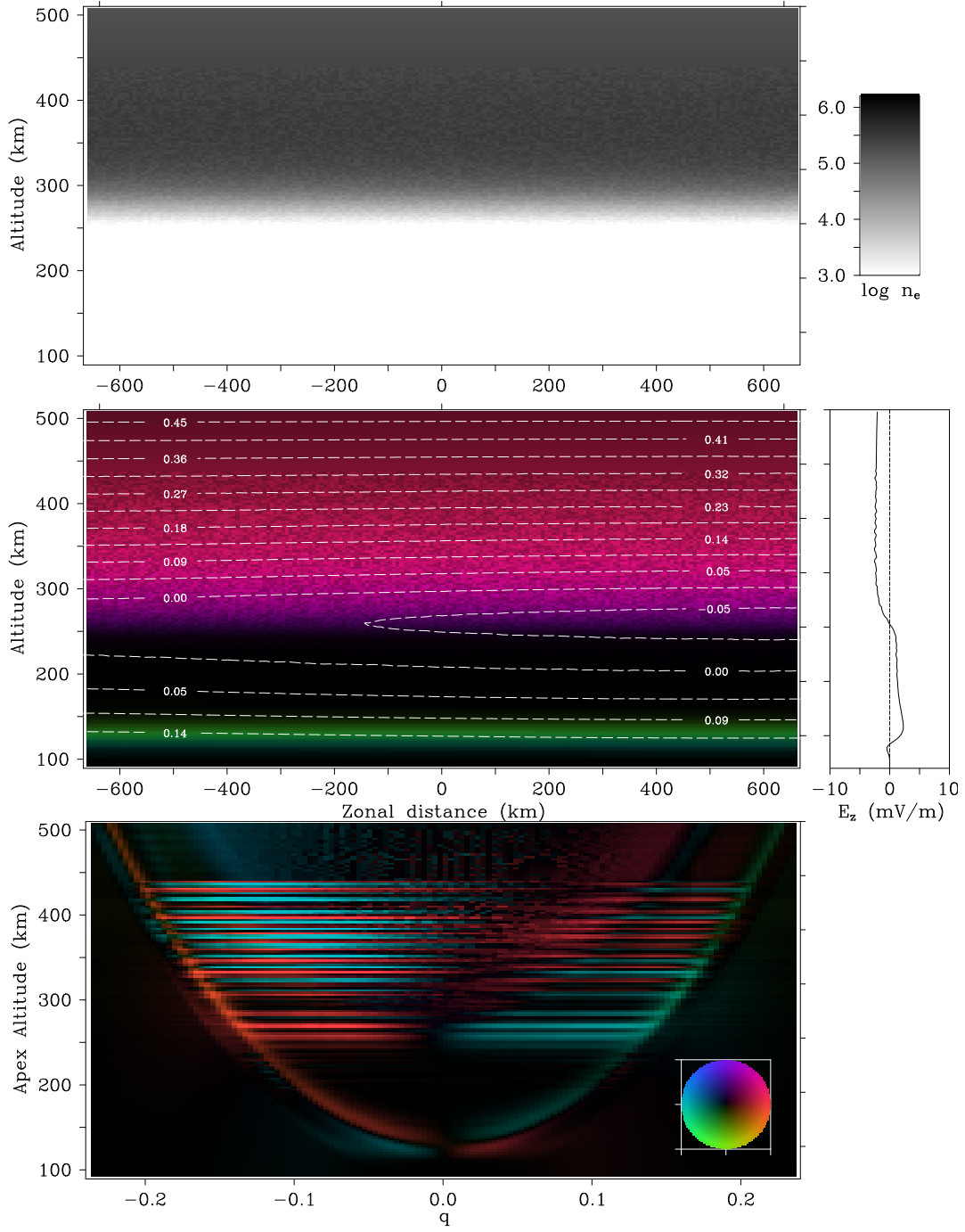
Figure 3: Initial conditions for ESF model run. Top: Plasma number density. Middle: Transverse current density in the equatorial plane with equipotential contours (in kV) superimposed in white. Middle right: vertical electric field. Bottom: current density in the meridional plane. The current densities are vector quantities with magnitudes and directions indicated by the color wheel at the bottom right. The maximum scale is 3 nA/m^2 in the equatorial plane and 30 nA/m^2 in the meridional plane. Note that diamagnetic currents are not represented in this diagnostic figure.
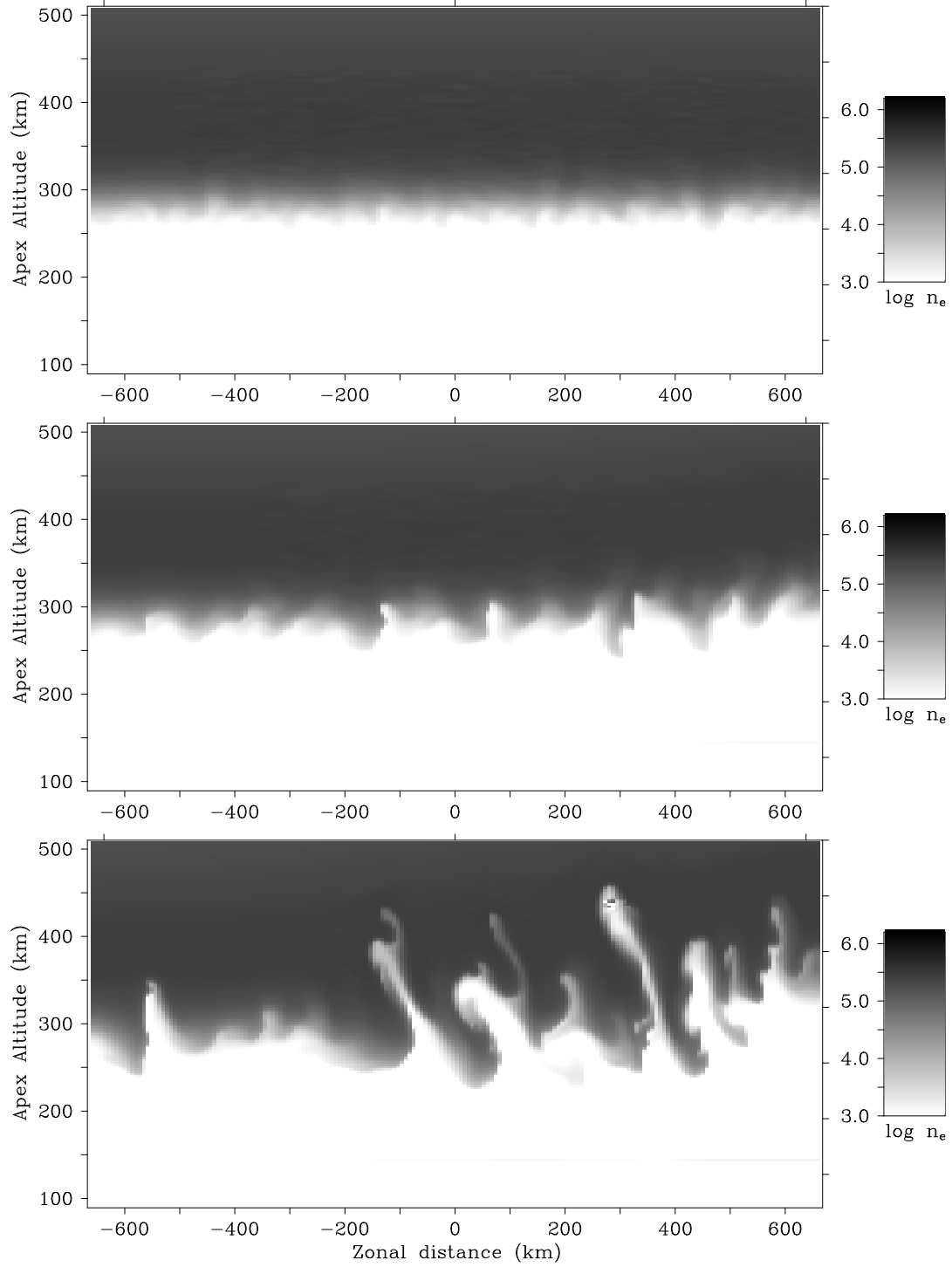
Figure 4: Simulated plasma densities in a cut through the Kwajalein latitudinal plane. The three panels show results for simulation times of 0h35m, 1h10m, and 1h43m, respectively, after a start time $t_\circ = 9{:}30$ UT (LT = UT + 11 hr at the horizontal center of the simulation).
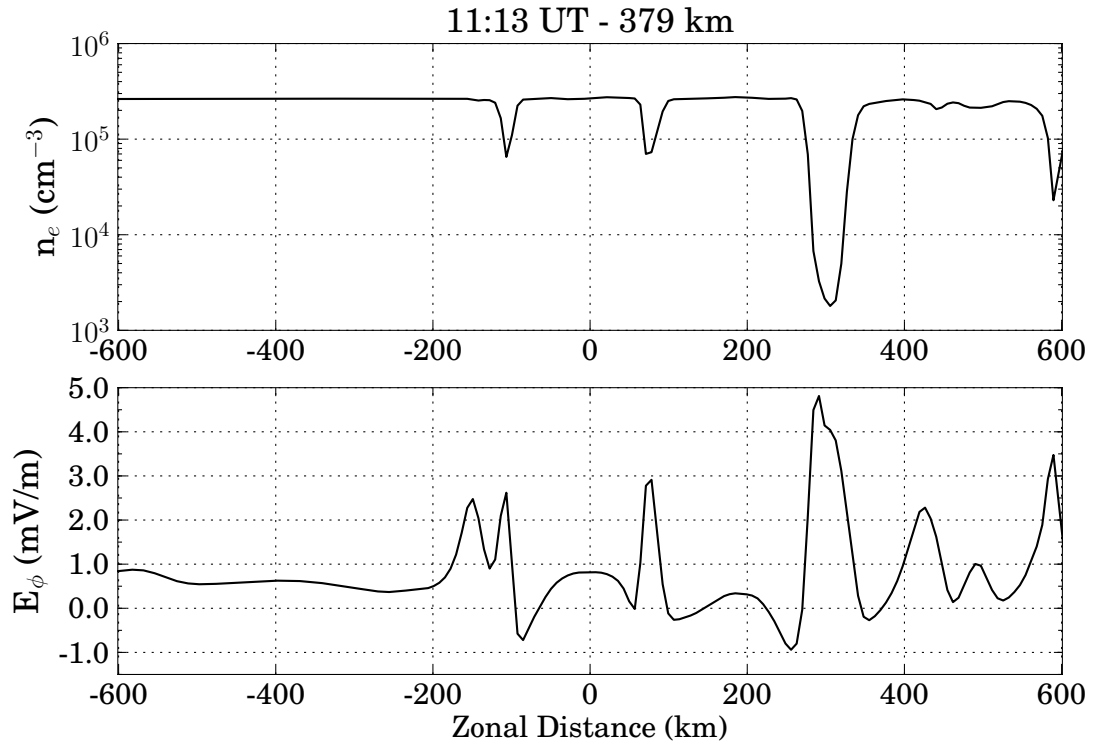
Figure 5: Electron density (cm^{-3}) and zonal electric field (mV/m) at 11:13 UT obtained from a longitudinal cut through the simulation at 379 km altitude over the Kwajalein sector ($\sim$400 km apex altitude).

was observed in ALTAIR scans and simulation results.

The transient response of CSI explained $\sim$ 30-50 km wave observations, a feature commonly observed by backscatter scatter radars in the form of patchy bottom-type ESF. These intermediate-scale irregularities were observed initially in both the simulations and the radar observations but did not reappear after they coalesced into emergent 100 km+ scale irregularities. This result agrees with observations made at other longitudinal sectors, e.g., at Jicamarca [*Hysell*, 2000].

During the asymptotic growth phase, when intermediate-scale depletions dominated the scenario, some of the irregularities remained confined to the bottomside, while others experienced more vertical development. Had these irregularities been observed with coherent scatter, e.g. by the Jicamarca radar, they would have been labeled bottomside ESF. The irregularities in the middle panels of the simulation (Figure 4b) and radar data (Figure 1b) are comparable in terms of scale sizes and altitude spans.

The last stage of development of ESF occurred when the vertical extension of the plasma depletion was large enough that the irregularities crossed through the peak into the topside. Similar features are observed in both the simulation (Figure 4c) and the radar data (Figure 1c). Depletions that reached the F peak were spaced by hundreds of km and displayed tilts close to 30° westward from zenith.

Measurements made by IVM showed that electric field perturbations of the order of a few mV/m were sometimes observed even when depletions in the densities were not detected. Similar features were present in the simulation and seemed to be a natural characteristic of the ESF morphology. The simultaneous measurements of small relative perturbations in the density and large zonal electric field perturbations seems to be a consequence of a satellite pass near the top of a plasma depletion. Since the depletion itself was not intercepted, it was not observed, but the fringing fields penetrated to higher altitudes and were detected.

Zonal neutral winds in the bottomside and valley regions exerted control over initial irregularity formation. This sensitivity to the winds was expected, since the growth rate of the collisional shear instability depends on the counter streaming flow of the neutrals and plasma [*Hysell et al.*, 2006]. As wind measurements in the lower thermosphere and mesosphere show considerable variability [*Larsen*, 2002], sensitivity tests to winds at those altitudes need to be performed to evaluate their effects on ESF initiation.

Conclusions

The combination of generalized Rayleigh Taylor and collisional shear instability produced growing waveforms with characteristics matching satellite and radar observations in terms of their gross morphology and rates of development. Growing intermediate- ($\sim$30 km) and large-scale (100+ km) waves resulted from the nonlocal and non-normal characteristics of the system and were not imposed a priori. The transient response of CSI explained rapid intermediate-scale wave emergence at the base of the F region, whereas the steady-state behavior seemed to account for the large-scale waves that ultimately dominated. The three different types of ESF (bottom-type, bottomside, and topside) appeared to be a result of the time sequencing of the transient and steady-state response of CSI in relation to the zonal electric field.

A major objective of this research was to simulate the electrodynamics of ionospheric plasma irregularities, including those in ESF, in the direction parallel to the geomagnetic field. The results of ESF simulation presented here suggests that a full 3-D treatment is necessary in order to track the distribution of parallel currents and the parallel closure of currents forced by dynamos. Parallel currents are found to have effects on the overall circulation and contribute to ESF morphology. Studies are underway to quantify the effects and mechanisms at work. Parallel currents are also necessary to account for spaceborne magnetometer measurements, such as those produced routinely by the CHAMP satellite during ESF encounters. Such measurements complement the kind of in situ measurements provided by C/NOFS and provide a rather complete specification of the irregularities and associated electrodynamics that constitute ESF. Our fully three-dimensional numerical model and analysis of ESF appears to be able to reproduce all of the salient features in the combined satellite and ground-based radar datasets.

Bibliography

Aveiro, H. C., and D. L. Hysell, Three-dimensional numerical simulation of equatorial F-region plasma irregularities with bottomside shear flow, *J. Geophys. Res.*, *115, A11321*, doi:10.1029/2010JA015,602, 2010.

Aveiro, H. C., D. L. Hysell, J. Park, and H. Luhr, Equatorial spread F-related currents: Three-dimensional simulations and observations, *Geophys. Res. Lett.*, *38, L21103*, 2011.

Bilitza, D., and B. W. Reinisch, International Reference Ionosphere 2007: Improvements and new parameters, *Adv. Space Res.*, *42*, 599–609, 2008.

Daniell, R. E., L. D. Brown, D. N. Anderson, M. W. Fox, P. H. Doherty, D. T. Decker, J. J. Sojka, and R. W. Schunk, PIM: a global parameterization based on first principles models, *Radio Sci.*, *30*, 1499, 1995.

Drake, J. F., and J. D. Huba, Dynamics of three-dimensional ionospheric plasma clouds, *Geophys. Res. Lett.*, *58 (3)*, 278–281, 1987.

Drake, J. F., M. Mulbrandon, and J. D. Huba, Three-dimensional equilibrium and stability of ionospheric plasma clouds, *Phys. Fluids*, *31 (11)*, 3412–3424, 1988.

Drob, D. P., An empirical model of the Earth's horizontal wind fields: HWM07, *J. Geophys. Res.*, *113, A12304*, doi:10.1029/2008JA013,668, 2008.

Huba, J. D., and S. L. Ossakow, On the generation of 3-m irregularities during equatorial spread F by low-frequency drift waves, *J. Geophys. Res.*, *84*, 6697, 1979.

Hysell, D. L., A review and synthesis of plasma irregularities in equatorial spread F, *J. Atmos. Sol. Terr. Phys.*, *62*, 1037, 2000.

Hysell, D. L., J. L. Chau, and C. G. Fesen, Effects of large horizonbtal winds on the equatorial electrojet, *J. Geophys. Res.*, *107*, doi:10.1029/2001JA000,217, 2002.

Hysell, D. L., J. Chun, and J. L. Chau, Bottom-type scattering layers and equatorial spread F, *Ann. Geophys.*, *22*, 4061, 2004.

Hysell, D. L., M. F. Larsen, C. M. S. A. Barjatya, T. F. Wheeler, T. W. Bullett, R. F. W. M. F. Sarango, J. L. Chau, and D. Sponseller, Rocket and radar investigation of background electrodynamics and bottom-type scattering layers at the onset of equatorial spread F, *Ann. Geophys.*, *24*, 1387–1400, 2006.

Kelley, M. C., *The Earth's Ionosphere; Plasma Physics and Electrodynamics*, Academic, San Diego, Calif., 2009.

LaBelle, J., M. C. Kelley, and C. E. Seyler, An analysis of the role of drift waves in equatorial spread F, *J. Geophys. Res.*, *91*, 5513, 1986.

Larsen, M. F., Winds and shears in the mesosphere and lower thermosphere: Results from four decades of chemical release wind measurements, *J. Geophys. Res.*, *107(A8)*, 1216, doi:10.1029/2001JA000,218, 2002.

Picone, J. M., A. E. Hedin, D. P. Drob, and A. C. Aikin, NRLMSISE-00 empirical model of the atmosphere: Statistical comparisons and scientific issues, *J. Geophys. Res.*, *107, A12*, doi: 10.1029/2002JA009,430, 2002.

Retterer, J. M., Physics based forecasts of equatorial radio scintillation for the Communication and Navigation Outage Forecasting System (C/NOFS), *Space Weather*, *3*, doi:10.1029/2005SW000,146, 2005.

Retterer, J. M., D. T. Decker, W. S. Borer, R. E. Daniell Jr., and B. G. Fejer, Assimilative modeling of the equatorial ionosphere for scintillation forecasting: Modeling with vertical drifts, *J. Geophys. Res.*, *110*, A11,307, doi:10.1029/2002JA009,613, 2005.

Richmond, A. D., Numerical model of the equatorial electrojet, *Tech. Rep. AFCRL-72-0668, ERP 421*, Air Force Cambridge Research Lab., Hanscom AFB, Bedford, MA, 1972.

Saad, Y., SPARSKIT : A basic tool kit for sparse matrix computations, *Tech. Rep. RIACS-90-20*, Research Institute for Advanced Computer Science, NASA Ames Research Center, Moffett Field, CA, 1990.

Shume, E. B., D. L. Hysell, and J. L. Chau, Zonal wind velocity profiles in the equatorial electrojet derived from phase velocities of type II radar echoes, *J. Geophys. Res.*, *110*, A12,308, doi:10.1029/2005JA011,210, 2005.

Trac, H., and U. L. Pen, A primer on Eulerian computational fluid dynamics for astrophysicists, *Astrophysics*, *115*, 303–321, 2003.

Tsunoda, R. T., M. J. Barons, J. Owen, and D. M. Towle, Altair: An incoherent scatter radar for equatorial spread *F* studies, *Radio Sci.*, *14*, 1111, 1979.

van der Vorst, H., Bi-CGSTAB: A fast and smoothly converging variant of Bi-CG for the solution of non-symmetric linear systems, *SIAM J. Sci. Statist. Comput.*, *13*, 631–644, 1992.

Zalesak, S. T., J. F. Drake, and J. D. Huba, Three-dimensional simulation study of ionospheric plasma clouds, *Geophys. Res. Lett.*, *17 (10)*, 1597–1600, 1990.